Research Square

Preprints are preliminary reports that have not undergone peer review.
They should not be considered conclusive, used to inform clinical practice,
or referenced by the media as validated information.

Monolithic gain–storage separation in low-noise supercavity lasers

Zhiting Tang
University of Electronic Science and Technology of China
Chuanlin Li
University of Electronic Science and Technology of China
Feiyun Zhao
Southwest Institute of Technical Physics
Aobo Ren
University of Electronic Science and Technology of China
Wuyang Ren
University of Electronic Science and Technology of China
Chuang Li
University of Electronic Science and Technology of China
Kai Shen
University of Electronic Science and Technology of China
Jiang Wu
jiangwu@uestc.edu.cn

University of Electronic Science and Technology of China

Article

Keywords:

Posted Date: November 9th, 2026

DOI: https://doi.org/10.21203/rs.3.rs-11571033/v1

License: This work is licensed under a Creative Commons Attribution 4.0 International License.
Read Full License

Additional Declarations: No competing interests reported.

Monolithic gain–storage separation in low-noise supercavity lasers

Zhiting Tang[1,6], Chuanlin Li[1,2,6], Feiyun Zhao[3], Aobo Ren[1*], Wuyang Ren[1], Chuang Li[1], Kai Shen[1], Jiang Wu[1,4,5*]

[1]Institute of Fundamental and Frontier Sciences, University of Electronic Science and Technology of China, Chengdu 611731, China

[2]National Key Laboratory on Advanced Laser and High Power Microwave, Mianyang 621900, China

[3]Southwest Institute of Technical Physics, Chengdu 610041, China

[4]State Key Laboratory of Electronic Thin Films and Integrated Devices, University of Electronic Science and Technology of China, Chengdu 611731, China.

[5]Mozi Laboratory, Zhengzhou 450001, China.

[6]These authors contributed equally: Zhiting Tang, Chuanlin Li

Email: aobo.ren@uestc.edu.cn; jiangwu@uestc.edu.cn

Abstract

Vertical-cavity surface-emitting lasers offer low power and wafer-scale integration, but their short cavities confine optical gain and photon storage to the same active region, limiting photon lifetime and spectral coherence. Here we propose a monolithic surface-emitting supercavity laser that functionally decouples optical gain from photon storage by coupling an active cavity to multiple passive storage cavities. Controlled intercavity coupling is achieved through precise engineering of the reflection, transmission, and phase matching of the connecting DBR mirrors. By tailoring the supermode profile and coherently redistributing its optical field among the active and passive cavities, we demonstrate a monolithic surface-emitting supercavity laser with an enlarged effective photon-storage volume and reduced noise. The coupled cavities yield a quality factor of 22,499 and a cold-cavity photon lifetime of 20.1 ps, while the supercavity laser retains low-threshold single-mode operation, a Lorentzian linewidth of 0.41 MHz, a frequency-noise floor of 2.0×10^5 Hz^2 Hz^{-1} and a high-frequency relative-intensity-noise floor near -145 dBc Hz^{-1} without external feedback. When the laser is locked to a Cs reference, the atomic-clock testbed reaches an Allan deviation of 8.7×10^{-13} at 8,192 s. This architecture establishes gain–storage separation as a scalable route to coherent surface emitters.

Introduction

Surface-emitting semiconductor lasers, particularly vertical-cavity surface-emitting lasers (VCSELs), provide compact, scalable and manufacturable light sources for integrated photonic systems[1,2]. Their wafer-normal emission enables wafer-level testing[3], low-threshold operation[4,5], near-circular beams[6,7] and dense two-dimensional arrays[8,9], supporting applications ranging from optical interconnects[10] and three-dimensional sensing[11,12] to chip-scale atomic systems and precision quantum measurements[13–16]. Yet the short vertical cavity that underpins these advantages also restricts photon residence and, consequently, the coherence of free-running VCSELs[17–22].

In a conventional VCSEL, a resonant cavity only a few optical wavelengths long is bounded by highly reflective distributed Bragg reflectors (DBRs), which compensate for the limited single-pass gain. The resulting mirror loss per unit optical length limits the photon lifetime. Multiple quantum wells (MQWs) are positioned at standing-wave antinodes to maximize modal gain[23–25], but this strong field-gain overlap also gives the active region a large participation in the lasing mode. Spontaneous emission and carrier-density-induced fluctuations in gain and refractive index therefore project efficiently onto the amplitude and phase of the optical field, increasing relative intensity noise (RIN), frequency noise and linewidth[26].

VCSEL coherence has been improved through external-cavity feedback[27–29], self-injection locking to high-Q resonators[30], coupled-resonator schemes[18,31] and electronic frequency stabilization. Although effective, these approaches commonly require external optics, precise coupling, active control or complex packaging, reducing the compactness, manufacturability and array compatibility of the platform[18]. Monolithic cavity engineering provides a more scalable route, and coupled-resonator VCSELs[18] have previously shown that a passive cavity can modify the optical field distribution, extend the effective cavity length and improve modal selectivity. However, these approaches have treated the passive resonator as an additional cavity for extending photon residence or tailoring intercavity dynamics, rather than as a controlled degree of freedom for engineering the regional participation of the lasing mode. Simply increasing the effective cavity length also introduces a fundamental trade-off: although the photon lifetime can be increased, the free spectral range (FSR) is reduced, increasing the

susceptibility to longitudinal-mode competition. A remaining challenge is therefore to control how optical energy is partitioned between the active region and passive photon-storage regions while preserving sufficient modal gain and robust longitudinal-mode discrimination. This requires a cavity architecture in which the spatial mode volume, effective photon lifetime and active-region noise participation can be simultaneously tailored through the intercavity coupling.

Here we demonstrate a monolithically integrated surface-emitting supercavity laser that provides multiple degrees of freedom for gain–storage engineering within the VCSEL platform. The supercavity incorporates multiple passive cavities, enabling precise control over the optical-field distribution. Phase-engineered DBR interfaces couple an MQW active cavity to passive photon-storage cavities, redistributing the optical mode, increasing its effective storage volume and extending the effective photon lifetime while retaining sufficient gain overlap. We establish how the complex intercavity coupling controls regional mode-volume contributions, quality factor and longitudinal-mode selection, and implement the resulting architecture in an electrically injected three-cavity VCSEL. The device combines sub-megahertz linewidth with low intensity noise and long-term Cs-referenced frequency stability.

Gain–storage separation in supercavity lasers

Conventional VCSELs confine the lasing field to a short Fabry-Pérot active cavity bounded by DBRs, with MQWs positioned near longitudinal-field antinodes to provide modal gain (Fig. 1a). This arrangement supports efficient stimulated emission and low-threshold operation, but it also co-locates gain and photon storage, giving the MQW region a substantial weighting in the optical mode. The coherence of the laser is therefore directly exposed to fluctuations generated in the active medium.

Carrier-population fluctuations perturb both material gain and refractive index, whereas spontaneous emission injects randomly phased photons into the lasing mode. Both processes contribute to the amplitude and phase quadratures of the optical field (Fig. 1b): amplitude fluctuations appear as RIN, while phase fluctuations produce frequency noise and linewidth broadening[32]. Because carrier-induced gain and index changes are linked through the linewidth-enhancement factor, their impact depends not only on the fluctuation strength but also on the optical weighting of the MQW region[26].

The spatial extent and regional weighting of the resonant field can be quantified using the effective mode volume[33],

$$V_{eff} = \frac{\int_{\Omega} \varepsilon(r)|E(r)|^2 d^3r}{\max_{r\in\Omega}[\varepsilon(r)|E(r)|^2]} \quad (1)$$

where E is the electric field, ε is the permittivity, r is the distance from the bottom, Ω covers the complete resonant structure, and the denominator is the global maximum of the electric-field energy-density weighting. In a VCSEL, Ω includes the active cavity and the relevant DBR penetration regions (Fig. 1c). Extending the active cavity can increase the round-trip time and distribute the field over a larger volume while the MQW thickness remains nearly fixed, reducing the MQW contribution. Gain interaction and photon storage, however, remain governed by the same longitudinal mode. The MQW overlap required for threshold operation, therefore, limits further dilution of active-region participation, while excessive cavity extension reduces the FSR and promotes longitudinal-mode competition.

To decouple these functions, we introduce a monolithically integrated surface-emitting supercavity comprising an MQW-containing active cavity and multiple passive cavities connected through phase-engineered DBR interfaces (Fig. 1e). Compared with a two-cavity coupled resonator, the multiple-cavity architecture introduces additional resonant sections and coupling interfaces, providing extra structural degrees of freedom to regulate optical-field partitioning and photon storage. Rather than relying on a single passive cavity or simply extending the cavity length, photon storage can be distributed across successive passive resonators while retaining control over the longitudinal-mode spectrum. The active cavity supplies modal gain, whereas the passive cavities add resonant volumes for photon storage without introducing additional gain media. For the complete structure, Ω extends across the active cavity, all passive cavities, the phase sections and the intervening DBRs, including their penetration regions. Regional mode-volume contributions are evaluated using the same global normalization, allowing the active- and passive-cavity contributions to be compared directly. The resulting optical-field distribution is governed by the DBR-pair design, which redistributes the lasing supermode between the active and passive cavities (Supplementary Fig. 1(a)-(b)).

At the target wavelength, each active cavity or passive cavity is designed to satisfy a round-trip phase close to $2m\pi$, whereas the intervening phase section provides the relative phase

required at the coupling interface, typically through a half-wave optical thickness. The phase section is not an additional storage cavity; rather, it regulates the phase relation between fields transmitted and reflected by the intermediate DBRs. The DBR-pair allocation and phase-section thickness jointly determine the complex intercavity coupling coefficient κ, including both its magnitude $|\kappa|$ and phase.

Tuning κ redistributes the coupled-cavity mode from the active cavity towards the passive cavities while retaining sufficient field intensity in the MQWs for lasing (Fig. 1f). The reduced active-cavity contribution dilutes the weighting of carrier and spontaneous-emission noise in the complete optical mode[34], whereas the passive cavities increase the volume available for photon storage. Partial transmission and reflection at successive interfaces establish cascaded feedback paths described by the ordered transfer matrices M_1, M_2, …, M_n[35] (see Supplementary Fig. 3). Their product determines the amplitude response, phase evolution, resonance condition and spatial field distribution of the active cavity-passive cavity system. Repeated circulation through these paths increases the effective residence length and photon lifetime, providing separate structural control over gain overlap, noise participation and photon storage.

Principle of supercavity mode redistribution

The phase-engineered coupling DBR is the key element that converts gain–storage separation into a controllable coupled-cavity field distribution. Each interface comprises left and right DBR segments containing L_p and R_p pairs, respectively, separated by a half-wave phase section (Fig. 2a). Redistributing the DBR pairs modifies the interface reflectivity, transmission, penetration depth and complex coupling coefficient κ. We therefore mapped $|\kappa|$ over the design space $5 \leq L_p + R_p \leq 60$ (see Supplementary Table 1).

The $T = 0.2$ and $T = 0.8$ contours divide the parameter space into three coupling regimes in Fig. 2a, where T is the transmissivity of the phase-engineered coupling DBR. Region I corresponds to a highly reflective interface, for which adjacent cavities are weakly coupled and the field remains largely confined to one resonant section (see Supplementary Table 2 for reflectivity). Region III is highly transmissive; the resulting overcoupling weakens the local feedback required to sustain distinct Fabry-Pérot resonances. Region II retains both intercavity transmission and local resonant feedback and therefore defines the practical design window.

Within this region, DBR-pair redistribution tunes $|\kappa|$ over a broad range and regulates the exchange of optical energy between neighbouring cavities.

Three representative designs, labelled I–III in Fig. 2a, show how the interface redistributes the longitudinal standing-wave field (Fig. 2b). An asymmetric allocation with fewer DBR pairs on the active cavity side and more on the passive cavity side shifts the field towards the passive cavity; reversing the allocation produces the opposite distribution, whereas a near-symmetric interface yields more comparable field amplitudes. The coupling DBR therefore acts not only as a partially reflecting mirror: its asymmetric layer distribution sets the reflection amplitudes and penetration depths on either side of the phase section, thereby controlling the spatial composition of the coupled-cavity mode.

We quantified this redistribution using the effective mode volume defined in Fig. 1, integrating over the active cavity, passive cavities, phase sections and relevant DBR penetration regions with a common global normalization. The passive-to-active mode-volume ratio, V_{PC}/V_{AC}, can be tuned from 0.09 to 10.59 through asymmetric DBR-pair allocation (Fig. 2c), indicating a substantial reduction in the relative active-cavity weighting. A large ratio, however, can arise from suppression of the active cavity contribution rather than maximum absolute storage in the passive cavities. We therefore also evaluate the mean normalized passive-cavity contribution, $\Sigma V_{PC}/n$, which peaks at approximately 1 near the symmetric allocation (Fig. 2d). Strong asymmetry minimizes active-region participation, whereas near-symmetric allocation maximizes the average passive-cavity contribution; the selected design balances these effects while preserving sufficient MQW field intensity for threshold gain.

Figure 2e resolves the coupling strength and phase responses of the phase-engineered interface. Changing the phase-section optical thickness shifts the relative phase of the transmitted and reflected fields, whereas the DBR-pair allocation primarily controls the coupling amplitude and field penetration. These parameters jointly define the complex κ and must therefore be optimized as a single interface response rather than treated as independent controls.

Mode redistribution also changes the storage dynamics of the complete resonator. As passive cavities are added, the calculated cold-cavity resonance narrows from 30.0 to 21.4 pm (Fig. 2f), consistent with increased stored optical energy and a longer effective photon residence time. Each coupling DBR provides partial reflection and transmission, and successive interfaces

form cascaded feedback paths between the active cavity and passive cavities. Repeated circulation through these paths increases the effective number of round trips before energy leaves the resonator, thereby extending the effective photon lifetime without an external cavity. The quality-factor analysis further quantifies the enhanced photon storage enabled by cavity cascading (Fig. 2g–i). The intrinsic quality factor Q_i accounts for absorption, scattering and other internal losses, whereas the external quality factor Q_e describes leakage through the terminal output channels of the complete resonator. The intermediate DBRs instead serve as internal coupling interfaces that redistribute optical energy between neighbouring cavities (Supplementary Fig. 4(a)-(e)).

Increasing the number of coupled cavities increases Q_{total} by introducing additional passive storage volumes and intercavity feedback paths. In the two-cavity structure, Q_e and Q_{total} are primarily governed by $\kappa_{1,2}$, which controls field transfer from the active cavity into the first passive cavity. Cascading a second passive cavity introduces an additional coupling degree of freedom through $\kappa_{2,3}$ and further increases Q_e and Q_{total}, while Q_i remains near 5.0×10^4. Across the investigated design space, Q_{total} reaches 23,380. As a proof of concept, we selected a three-cavity architecture comprising one active cavity and two cascaded passive cavities, which achieves Q_{total} = 22,499 (Supplementary Table 3(a)-(c)), corresponding to a cold-cavity photon lifetime of approximately 20.1 ps, compared with 2.5 ps for the reference condition. The corresponding cold-cavity spectra are shown in Supplementary Fig. 5(a)-(e).

Cavity cascading also enriches the longitudinal eigenstate structure of the coupled resonator (Fig. 2j), making longitudinal-mode discrimination an additional design consideration as the number of resonant sections increases. The three-cavity configuration used here retains clear spectral separation around the target resonance while providing two independently designed coupling interfaces for redistributing the optical field into the passive cavities. This architecture was therefore adopted for the proof-of-concept device, combining enhanced photon storage, reduced active-region participation and robust longitudinal-mode selection (Fig. 2k), with an effective FSR of approximately 9.4 nm (Supplementary Fig. 6).

Device implementation and optoelectronic performance

The three-cavity design was implemented in a monolithic VCSEL comprising one MQW-containing active cavity and two passive cavities, PC_1 and PC_2. To retain sufficient modal gain

across the operating-temperature range while allowing the coupled-cavity structure to select the lasing wavelength, the target resonance was placed on the red side of the room-temperature gain maximum (Fig. 3a), with a nominal detuning[36] of approximately 14.5 nm. The fabricated wafer exhibits a photoluminescence peak at 878.8 nm and a target reflectivity minimum at 891.03 nm, corresponding to a measured separation of approximately 12.2 nm (Fig. 3b). The agreement between simulated and measured reflectivity is consistent with preservation of the designed optical thicknesses during epitaxial growth. The target resonance remains within the MQW gain envelope and is spectrally separated from neighbouring longitudinal resonances, in accordance with the mode-selection criterion established in Fig. 2.

The devices were fabricated using a standard III-V VCSEL process (Supplementary Fig. 7). Cross-sectional scanning electron microscopy resolves the complete active cavity-PC_1-PC_2 stack, including the terminal DBRs, oxide-confinement layer, MQW region and two passive cavities (Fig. 3c). Magnified images resolve the $In_{0.135}Ga_{0.865}As/Al_{0.25}Ga_{0.75}As$ quantum wells and oxide aperture, and the top-view image shows the surface grating used for polarization selection. The nominal 3.5-μm oxide aperture defines the current-injection area and lateral confinement, whereas the grating introduces polarization-selective loss without disrupting the longitudinal photon-storage path.

The light–current–voltage characteristics show that the extended vertical stack preserves efficient electrical injection (Fig. 3d). The device has a threshold current of 0.45 mA, a maximum continuous-wave output power of 1.34 mW and a peak power-conversion efficiency of 15.75% (Supplementary Fig. 8); the orthogonal-polarization suppression ratio reaches 30.6 dB. These results show that redistribution of the optical field into PC_1 and PC_2 retains sufficient MQW overlap for efficient stimulated emission, while the surface grating provides stable polarization selection.

Continuous-wave lasing is maintained from 25 to 95 °C (Fig. 3e). The threshold current remains below 1.0 mA across this range and is approximately 0.5 mA at 95 °C. Output power and efficiency decrease at elevated temperature because of reduced material gain, increased carrier leakage and higher internal loss, without an abrupt threshold transition. The temperature-dependent *L-I* results of the 5-μm-aperture VCSELs between 25 and 95 °C are shown in Supplementary Fig. 9. Notably, the 5-μm-aperture devices still maintain single-mode

operation, in contrast to the higher-order transverse-mode competition typically observed in conventional VCSELs. Temperature-dependent spectra retain a single dominant longitudinal mode with a side-mode suppression ratio above 30 dB (Fig. 3f). The wavelength shifts at approximately $0.05\ \mathrm{nm\ K^{-1}}$ without hopping to an adjacent coupled-cavity eigenmode (Supplementary Fig. 10). The 5-μm-aperture device exhibits similar continuous-wave lasing characteristics (Supplementary Fig. 11), maintaining single-mode emission with a side-mode suppression ratio above 32 dB and a wavelength temperature coefficient of approximately $0.05\ \mathrm{nm\ K^{-1}}$.

The transverse-mode behaviour was examined using an effective-index fibre model, in which the oxide aperture is represented as a weakly guiding cylindrical waveguide (Fig. 3g). Redistribution of part of the longitudinal field from the oxide-confined active cavity into the passive sections reduces the effective overlap with the oxide layer and, consequently, the lateral effective-index contrast Δn_{eff} between the aperture core and cladding[23,37–41]. The model therefore predicts fewer supported LP modes and greater diffraction or leakage loss for higher-order modes, whose fields extend farther beyond the oxide boundary. The $\mathrm{LP_{01}}$ mode retains the strongest gain overlap and lowest modal loss, while its larger transverse extent is expected to narrow the far-field distribution. The measured far fields are consistent with this trend (Fig. 3h): devices with 3.5- and 5-μm apertures exhibit compact, approximately Gaussian profiles with divergence angles of 5.8°–7.6°. These results are consistent with passive cavity-assisted weakening of the effective lateral confinement and suppression of higher-order transverse modes.

Current-dependent spectra of the 3.5-μm-aperture device further demonstrate stable longitudinal-mode selection (Fig. 3i). Single-mode emission is maintained across the measured current range, with a maximum side-mode suppression ratio of approximately 25 dB at 3.5 mA. The lasing wavelength shifts at approximately $0.60\ \mathrm{nm\ mA^{-1}}$ (Supplementary Fig. 12), predominantly because of Joule heating and carrier-induced refractive-index changes, without abrupt mode switching. The electrical, thermal, spectral and far-field measurements therefore show that the three-cavity architecture retains low-threshold operation, stable polarization and robust transverse- and longitudinal-mode control. Consistent current-dependent single-mode

operation was also obtained from the 5-μm-aperture device (Supplementary Fig. 13), with an SMSR of ~20 dB at 2.5 mA and a wavelength tuning coefficient of 0.59 nm mA^{-1}.

Noise, linewidth and stability of the supercavity laser

Frequency-noise and RIN spectra were measured using a stabilized fibre-based system (Fig. 4a). One branch of the laser output was directed to a calibrated homodyne interferometric frequency discriminator, whose response was converted to the frequency-noise power spectral density $S\nu(f)$[42]. A second branch was routed through a stabilized optical chain for direct RIN acquisition. Independent temperature control of the laser and fibre paths reduced slow thermal and mechanical drift.

At an injection current of 1.5 mA, the frequency-noise spectrum decreases approximately as $1/f$ at low offset frequencies and approaches a white floor of 2.0×10^5 Hz^2 Hz^{-1} at high offsets (Fig. 4b). The low-frequency component contains technical and environmental perturbations, whereas the white floor represents the Lorentzian phase-diffusion contribution[43] and corresponds to an equivalent linewidth of 0.48 MHz. Observation-time-dependent linewidths obtained using the β-separation-line method are shown in Supplementary Fig. 14. The sub-megahertz white-noise linewidth is consistent with the reduced active-region weighting and extended effective photon lifetime of the selected three-cavity mode.

The RIN spectra measured at 25 and 85 °C nearly overlap across the measured bandwidth (Fig. 4c). At 25 °C, the RIN is -120.3 dBc Hz^{-1} at 100 Hz and -135.8 dBc Hz^{-1} at 10 kHz, approaching a high-frequency floor near -145 dBc Hz^{-1}. The floor remains below -142 dBc Hz^{-1} over the investigated operating range, without a pronounced relaxation-oscillation peak or excess-noise feature in the measured band. Current-dependent RIN spectra are provided in Supplementary Fig. 15. Combined with the frequency-noise result, these measurements indicate low phase and amplitude fluctuations of the coupled-cavity mode.

The Lorentzian linewidth was independently assessed by heterodyne beat-note measurements (Fig. 4d). The supercavity laser was combined with a calibrated narrow-linewidth reference laser, and the radio-frequency beat signal was recorded using an electrical signal analyser. Lorentzian fits to the spectra yield linewidths of 0.41 MHz at 25 °C and 0.47 MHz at 85 °C (Fig. 4e), in close agreement with the frequency-noise measurement. Additional temperature- and current-dependent spectra are presented in Supplementary Fig. 16. The small increase at

85 °C shows that the phase-engineered active cavity-passive cavity resonance retains sub-megahertz coherence under elevated-temperature operation.

The Lorentzian linewidth decreases with increasing optical power and is approximately linear in P^{-1} at both 25 and 85 °C (Fig. 4f), as expected for photon-number-dependent phase diffusion in semiconductor lasers. Relative to the reference device, the supercavity laser exhibits a smaller P^{-1} coefficient and a lower extrapolated linewidth, consistent with increased passive-cavity photon storage and reduced active-region noise weighting. The corresponding high-frequency white-RIN floor remains below -142 dBc Hz^{-1} across the measured current range at both temperatures (Fig. 4g), indicating low high-frequency intensity fluctuations and thermally robust operation.

Long-term stability was evaluated by integrating the supercavity laser into a Cs vapour-cell atomic-clock testbed (Fig. 4h). The transmitted atomic signal provided the error signal used to stabilize the 4.6-GHz microwave interrogation frequency, and the resulting 10-MHz clock output was compared with a Cs frequency standard[13]. Over 260,000 s, the optical-power record remains continuous, with a relative variation of only approximately 0.07%, corresponding to sub-10^{-3} power fluctuations over multi-day operation and thereby limiting power-induced light-shift fluctuations in the Cs reference (Fig. 4i). The fractional-frequency record remains continuously locked without abrupt excursions over the same period, with the total variation confined within approximately 6×10^{-10} (Fig. 4j). Residual slow variations on these timescales can also arise from the complete clock testbed, including the vapour-cell temperature, microwave chain and servo electronics, rather than from the optical source alone.

The Allan deviation[44] follows an approximately $\tau^{-1/2}$ dependence at short averaging times, decreasing from approximately 2.4×10^{-11} at 1 s to 1.2×10^{-12} at 1,000 s, before reaching a minimum of 8.7×10^{-13} at 8,192 s (Fig. 4k). This stability extends beyond that recently reported for a single-passive-cavity VCSEL-based Cs clock[22] and reaches the 10^{-13} regime achieved in optimized compact CPT-clock systems (Supplementary Fig. 17), demonstrating that the low-noise supercavity laser supports both short-term coherence and long-term Cs-referenced frequency stability.

Conclusion

We have demonstrated a monolithically integrated surface-emitting supercavity that separates optical gain from photon storage within the VCSEL epitaxial stack. Phase-engineered coupling DBRs redistribute the coupled-cavity mode from an MQW active cavity into two passive cavities, increasing the effective storage volume and photon lifetime while reducing the relative weighting of active-region noise. The selected three-cavity architecture balances this noise dilution against modal-gain overlap and longitudinal-mode discrimination, reaching a Q_{total} of 22,499 and an effective photon lifetime of 20.1 ps. The fabricated laser retains a threshold current of 0.45 mA, stable single-mode emission and controlled polarization, and exhibits a Lorentzian linewidth of 0.41 MHz, a frequency-noise floor of 2.0×10^5 $\mathrm{Hz^2\,Hz^{-1}}$ and a high-frequency RIN floor near -145 $\mathrm{dBc\,Hz^{-1}}$. Integrated into a Cs clock testbed, it operates continuously for 260,000 s and reaches an Allan deviation of 8.7×10^{-13} at 8,192 s. These results establish gain–storage separation through phase-engineered monolithic supercavities as a scalable route to compact, low-noise and frequency-stable surface emitters.

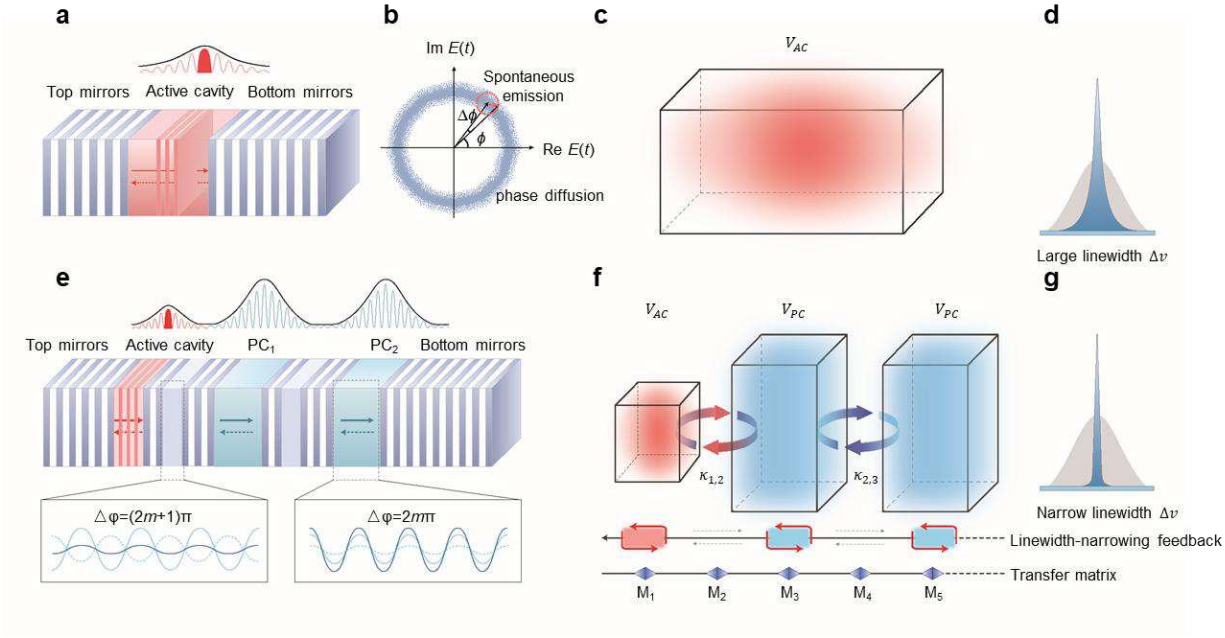


Figure 1 | Concept of gain–storage separation in a supercavity laser. a, Conventional VCSEL architecture. A short Fabry-Pérot active cavity bounded by DBRs, with multiple quantum wells (MQWs) positioned near standing-wave antinodes. **b**, Amplitude and phase quadratures of optical-field fluctuations. **c**, Effective active-cavity mode volume, V_{AC}. **d**, Strong active-region participation allows spontaneous-emission and carrier-induced refractive-index fluctuations to broaden the laser linewidth. **e**–**g**, Monolithic supercavity concept. **e**, An MQW-containing active cavity coupled to two passive photon-storage cavities (PC_1 and PC_2) through phase-engineered DBR interfaces. The cavity sections satisfy the constructive resonance condition ($\Delta\varphi = 2m\pi$), whereas the phase sections impose the relative phase condition ($\Delta\varphi = (2m+1)\pi$) required for intercavity coupling. **f**, Coupling coefficients $\kappa_{1,2}$ and $\kappa_{2,3}$ redistribute the optical field into the passive cavities. The interface responses are represented by the transfer matrices (M_1, M_2,…M_n), whose ordered product describes the cascaded feedback and field evolution of the complete resonator. **g**, Reduced active-region weighting and increased passive photon storage dilute phase noise and narrow the linewidth.

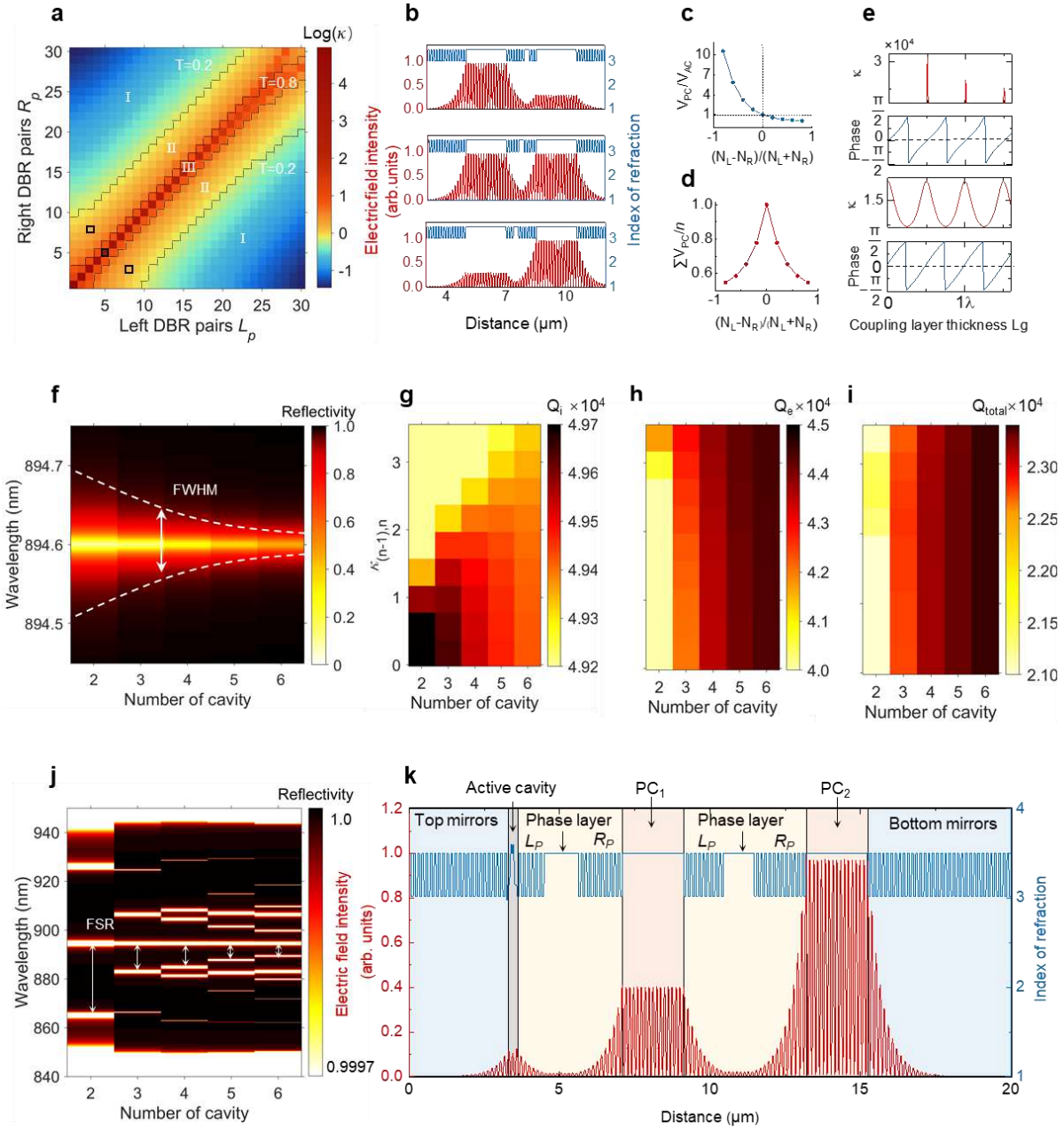


Figure 2 | Phase-engineered coupling DBRs for mode-volume and photon-lifetime control. **a**, Coupling strength $|\kappa|$ as a function of the left and right DBR-pair numbers, L_p and R_p, for $5 \leq L_p + R_p \leq 60$. The solid contours mark transmissivities of $T = 0.2$ and $T = 0.8$ and delimit the intermediate coupling regime. **b**, Standing-wave field distributions for representative designs I–III in **a**, showing redistribution between adjacent Fabry-Pérot cavities. **c**, Passive-to-active mode-volume ratio, V_{PC}/V_{AC}, tunable from 0.09 to 10.59. **d**, Mean normalized passive-cavity contribution, $\Sigma V_{PC}/n$, peaking near 1 for a near-symmetric DBR allocation. **e**, Coupling strength and phase responses as a function of phase-section optical thickness. **f**, Narrowing of

the cold-cavity resonance with increasing cavity number. **g**–**i**, Intrinsic quality factor Q_i (**g**), external quality factor Q_e (**h**) and total quality factor Q_{total} (**i**) as functions of cavity number and coupling strength $\kappa_{n-1,n}$. **j**, Evolution of the longitudinal eigenmode spectrum, showing increasingly dense supermode clusters as additional cavities are introduced. **k**, Refractive-index and standing-wave field distributions of the selected three-cavity design, which balances active-region noise dilution, passive photon storage and longitudinal-mode discrimination.

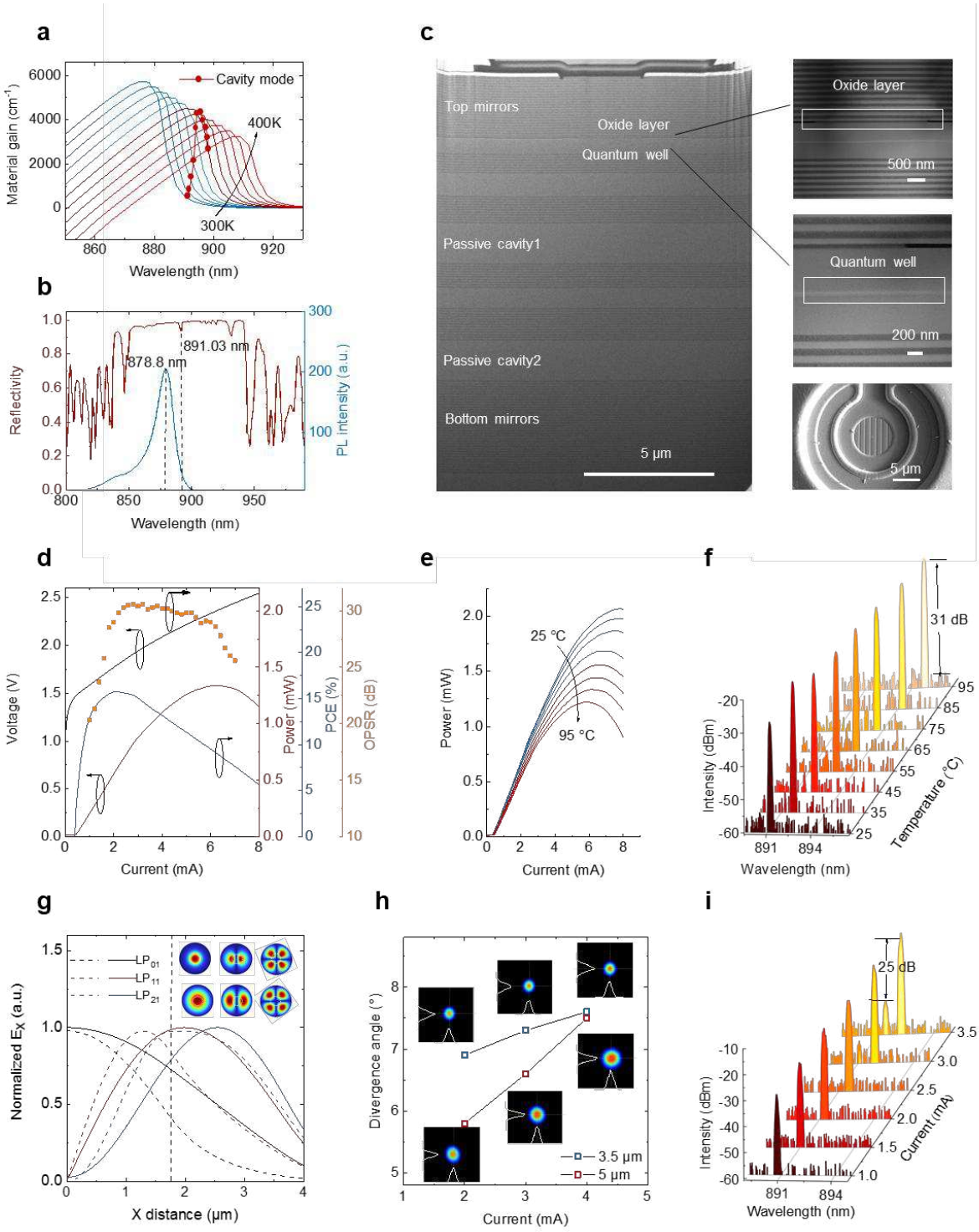


Figure 3 | Device implementation and optoelectronic performance. **a**, Temperature-dependent material-gain spectra and designed cavity resonance. **b**, Simulated and measured reflectivity spectra and room-temperature photoluminescence, showing a photoluminescence peak at 878.8 nm and target reflectivity minimum at 891.03 nm. **c**, Cross-sectional electron micrograph of the active cavity-PC_1-PC_2 stack, with magnified images of the oxide aperture

and MQW region and a top-view image of the surface grating. **d**, Light–current–voltage characteristics, power-conversion efficiency and orthogonal-polarization suppression ratio. **e**, Temperature-dependent light-current characteristics of a 3.5-μm-aperture device from 25 to 95 °C. **f**, Temperature-dependent emission spectra of a 3.5-μm-aperture device, retaining a side-mode suppression ratio above 31 dB. **g**, Calculated transverse-mode profiles and modal characteristics. **h**, Far-field profiles of devices with 3.5- and 5-μm apertures at different currents, with divergence angles of 5.8°–7.6°. **i**, Current-dependent spectra of the 3.5-μm-aperture device, showing single-mode emission with a maximum side-mode suppression ratio of approximately 25 dB.

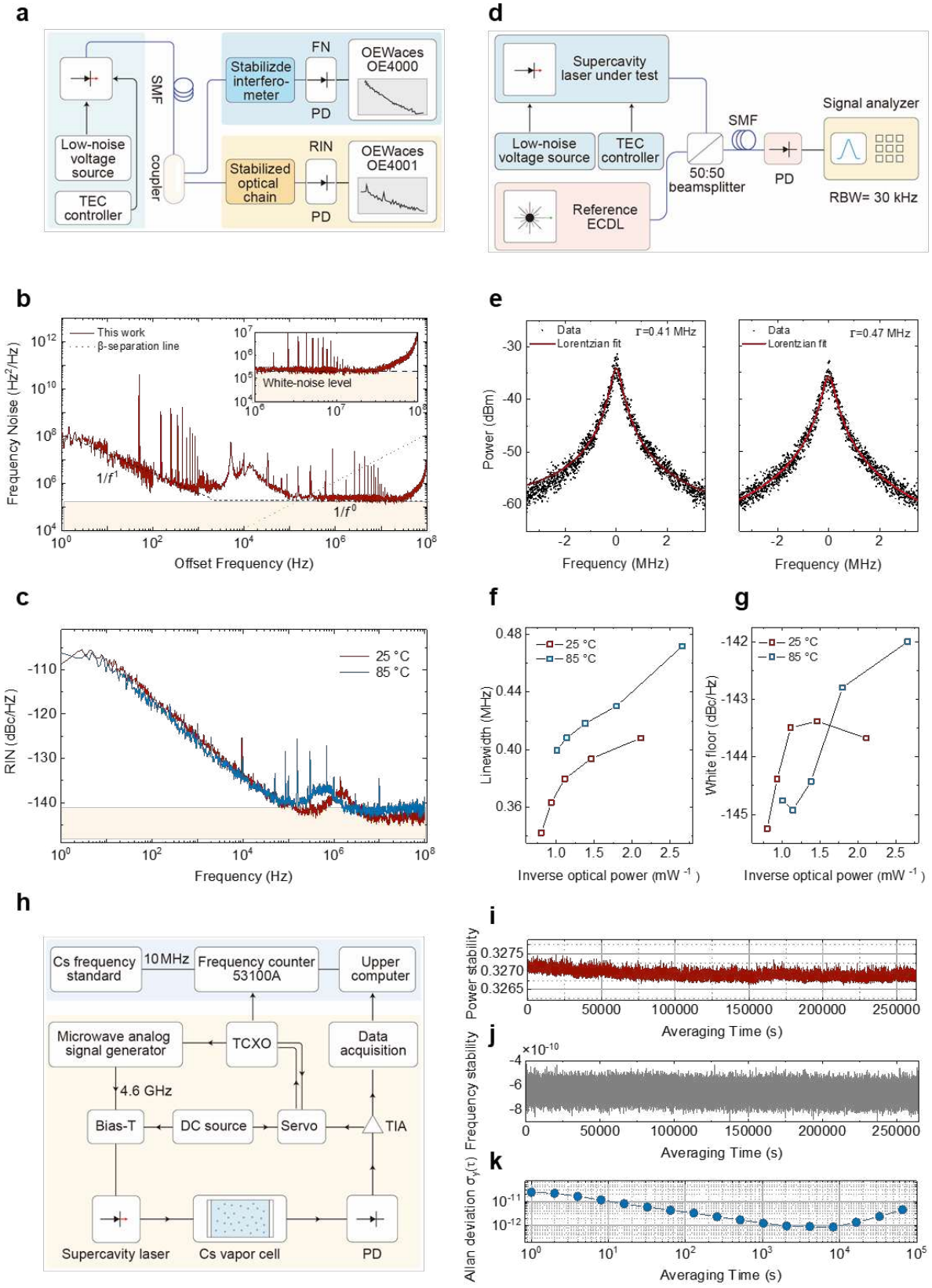


Figure 4 | Noise, linewidth and long-term stability of the supercavity laser. a, Stabilized-interferometer setup for frequency-noise and relative-intensity-noise (RIN) measurements. **b**,

Frequency-noise power spectral density; the inset highlights the high-offset-frequency white-noise floor, corresponding to an equivalent Lorentzian linewidth of 0.48 MHz. **c**, RIN spectra at 25 and 85 °C, approaching a high-frequency floor near -145 dBc Hz^{-1}. **d**, Heterodyne beat-note setup using a narrow-linewidth reference external-cavity diode laser. **e**, Beat-note spectra and Lorentzian fits at 25 and 85 °C, yielding linewidths of 0.41 and 0.47 MHz, respectively. **f**,**g**, Lorentzian linewidth (**f**) and high-frequency white-RIN floor (**g**) as functions of inverse optical power at 25 and 85 °C. **h**, Setup for long-term optical-power and Cs-clock-referenced frequency-stability measurements. **i**,**j**, Optical-power (**i**) and fractional-frequency (**j**) records over 260,000 s. **k**, Allan deviation of the Cs-clock testbed incorporating the supercavity laser, reaching 8.7×10^{-13} at an averaging time of 8,192 s.

Acknowledgements

This work was supported by the National Natural Science Foundation of China (62625403; 52472148), National Key Research and Development Program of China (2021YFA1401100). A.R. acknowledges the support from the TCL Young Scholars Program.

Author contributions

J.W. conceived the project, and A.R. and J.W. supervised the project. Z.T. conducted the experiments. Z.T., A.R. and J.W. coordinated the collaboration and were assisted by C.L.L., F.Z., W.R., K.S. and C.L. Z.T., C.L.L. and A.R. performed the measurements. Z.T., C.L.L. and A.R. analysed the data, designed the model and performed the theoretical derivations. Z.T. drafted the first version of the paper, with assistance from A.R. and J.W. All authors read and commented on, or contributed to the writing of, the manuscript.

Competing interests

The authors declare no competing interests.

Data availability

The data that support the findings of this study are available from the corresponding authors upon reasonable request.

Code availability

The code that supports the findings of this study is available from the corresponding authors upon reasonable request.

Correspondence and requests for materials should be addressed to A.R. or J.W.

Supplementary information

The online version contains supplementary material.

Methods

Optical simulations

To describe the optical response of the monolithic supercavity, a scattering-matrix formalism based on the secular equation was employed. As illustrated in Supplementary Fig. 2, the optical fields on the two sides of a coupling interface satisfy[35]

$$\begin{bmatrix} E_1^{'} \\ E_2^{'} \end{bmatrix} = \begin{bmatrix} S_{11} & S_{12} \\ S_{21} & S_{22} \end{bmatrix} \begin{bmatrix} E_1 \\ E_2 \end{bmatrix} \tag{2}$$

where S_{ij} are the effective scattering coefficients describing the reflection and transmission of the coupled-cavity interface.

The strength and phase of the intercavity interaction are characterized by the complex coupling coefficient,

$$C = \sqrt{\left(\frac{S_{12}S_{21}}{S_{11}S_{22}}\right)} = C_0 e^{i\theta} \tag{3}$$

where C_0 and θ represent the coupling amplitude and phase, respectively.

For a coupling region bounded by two distributed Bragg reflectors with reflection coefficients r_{b1} and r_{f2}, and transmission coefficients t_{b1} and t_{f2}, the effective scattering coefficients are obtained by summing all multiple reflections inside the coupling section, giving

$$S_{11} = -r_{b1} + \frac{r_{f2}t_{b1}^2 e^{-i2\beta_c l_c}}{1 - r_{b1}r_{f2}e^{-i2\beta_c l_c}} \tag{4}$$

$$S_{12} = \frac{t_{b1}t_{f2}e^{-i\beta_c l_c}}{1 - r_{b1}r_{f2}e^{-i2\beta_c l_c}} \tag{5}$$

$$S_{21} = \frac{t_{b1}t_{f2}e^{-i\beta_c l_c}}{1 - r_{b1}r_{f2}e^{-i2\beta_c l_c}} \tag{6}$$

$$S_{22} = -r_{f2} + \frac{r_{b1}t_{f2}^2 e^{-i2\beta_c l_c}}{1 - r_{b1}r_{f2}e^{-i2\beta_c l_c}} \tag{7}$$

where $\beta = n_c k_0 + i\alpha_c/2$ is the complex propagation constant of the coupling region, l_c is the coupling-layer thickness, n_c is the refractive index, and α_c is the gain (or loss) coefficient.

The same formalism can be extended recursively to cavities containing more than two resonators by replacing the downstream cavities with their effective reflection coefficients. For

example, in a three-cavity VCSEL, the third cavity and its coupling section are incorporated into an effective reflectivity,

$$r_3^{eff} = S_{22} + \frac{r_{b3}e^{-i2\beta_3 l_3}S_{23}S_{32}}{1 - r_{b3}e^{-i2\beta_3 l_3}S_{33}} = S_{22}\left(1 + \frac{C_2 r_{b3}e^{-i2\beta_3 l_3}S_{33}}{1 - r_{b3}e^{-i2\beta_3 l_3}S_{33}}\right) \quad (8)$$

The effective reflectivity can be generalized recursively to an arbitrary N-cavity cascaded structure, as given in Supplementary Eq. (1.16).

Finally, the cold-cavity reflectance spectrum is calculated from the effective reflection coefficient, and the corresponding cold-cavity linewidth is extracted by Lorentzian fitting of the resonance peak.

The transverse optical modes were calculated using an equivalent optical-fibre model. The effective refractive index of the VCSEL cavity was obtained by averaging the longitudinal refractive-index distribution with the corresponding electric-field intensity as a weighting function. The resulting effective refractive-index profile was then used to calculate the transverse modes LP_{01}, LP_{11}, and LP_{21}[39].

$$n_{eff} = \frac{\int n(z) * |E(z)|^2 dz}{\int |E(z)|^2 dz} \quad (9)$$

where n_{eff} is the effective refractive index, $n(z)$ is the refractive-index distribution along the longitudinal (z) direction, and $|E(z)|^2$ denotes the corresponding electric-field intensity.

The oxide aperture introduces a small effective refractive-index contrast difference between the oxidized and unoxidized regions, allowing the transverse optical confinement to be approximated as a weakly guiding cylindrical waveguide ($\Delta n_{eff} \ll n_{eff}$). Under this approximation, the vectorial eigenvalue problem reduces to a scalar linearly polarized mode formulation. The optical field of the supported LP_{mn} modes is expressed as

$$E_{mn}(r, \phi, z) \propto e^{jm\phi}e^{j\beta_{mn}z}J_m(u_{mn}r) \quad (10)$$

For $r < a$ (core), and

$$E_{mn}(r, \phi, z) \propto e^{jm\phi}e^{j\beta_{mn}z}K_m(v_{mn}r) \quad (11)$$

For $r > a$ (cladding), where a is the core radius, corresponding to half of the oxide-aperture diameter, and (r, ϕ, z) denote the cylindrical coordinates. Here, β_{mn} is the modal propagation constant, while J_m and K_m are the Bessel function of the first kind and the modified Bessel function of the second kind, respectively.

The transverse wavevector parameters inside and outside the waveguide core are defined as

$$u_{mn}^2 = k_0^2 n_{eff1}^2 - \beta_{mn}^2 \tag{12}$$

$$v_{mn}^2 = -\beta_{mn}^2 - k_0^2 n_{eff2}^2 \tag{13}$$

where k_0 is the free-space wavenumber, and n_{eff1} and n_{eff2} are the effective refractive indices of the core and cladding, respectively. Enforcing the continuity of the electromagnetic fields at the core-cladding interface leads to the characteristic equation[45]

$$u \cdot \frac{J_{m-1}(ua)}{J_m(ua)} = -v \frac{K_{\text{m-1}}(va)}{K_m(va)} \tag{14}$$

whose solutions determine the supported LP eigenmodes together with the corresponding modal propagation constants.

The quality factor[26] Q_{total} is determined by the combined contribution of intrinsic and external losses:

$$Q_{total}^{-1} = Q_i^{-1} + Q_e^{-1} \tag{15}$$

where Q_i and Q_e denote the intrinsic and external quality factors, respectively.

The internal quality factor is determined solely by optical losses inside the cavity, independent of mirror transmission and resonator coupling. Because the optical field is distributed across the active and passive cavities, the effective internal loss is determined by the optical-energy-weighted contributions from each region. Using the effective optical mode volumes (Eq. (1)), the internal quality factor is given by

$$Q_i^{-1} = \frac{\langle \alpha_a \rangle V_{AC} + \langle \alpha_p \rangle V_{PC}}{V_{total}} \frac{\lambda}{2\pi n_g} \tag{16}$$

where $\langle \alpha_a \rangle$ and $\langle \alpha_p \rangle$ denote the average optical losses in the active and passive cavities, respectively, n_g is the group refractive index, and λ is the resonance wavelength.

The external quality factor is extracted from the simulated cold-cavity resonance spectrum according to

$$Q_e^{-1} = \frac{\Delta\lambda}{\lambda_0} \tag{17}$$

where λ_0 is the resonance wavelength and $\Delta\lambda$ is the full width at half maximum (FWHM) of the resonance.

The cold-cavity photon lifetime[35] is then calculated from the external quality factor,

$$\tau_p = \frac{Q_e}{\omega_0} \tag{18}$$

where ω_0 is the angular resonance frequency. The above analysis was applied to coupled-cavity structures with varying numbers of passive photon-storage cavities and different intercavity coupling strengths to evaluate their quality factors and photon lifetimes.

To evaluate the thermal behaviour of the VCSEL under continuous-wave operation, a self-consistent electro-opto-thermal model with temperature-dependent material parameters was employed. The steady-state temperature distribution was obtained by solving the heat-diffusion equation

$$\nabla \cdot (k\nabla T) + H = 0 \tag{19}$$

where k is the thermal conductivity and H is the total volumetric heat-generation rate. The coupled electrical, optical, and thermal equations, incorporating Joule heating, optical absorption, carrier recombination, radiative energy transfer, and thermoelectric effects, were solved iteratively until convergence.

Epitaxial growth

The 894.6 nm supercavity VCSEL was grown on an n-type GaAs substrate by metal–organic chemical vapor deposition (MOCVD). The bottom mirror consists of 36 pairs of n-doped

quarter-wave $Al_{0.16}Ga_{0.84}As/Al_{0.92}Ga_{0.08}As$ DBRs. The active region comprises three 5-nm-thick $In_{0.135}Ga_{0.865}As$ quantum wells separated by 8-nm-thick $Al_{0.25}Ga_{0.75}As$ barriers. A 30-nm-thick $Al_{0.98}Ga_{0.02}As$ oxidation layer was positioned at the first standing-wave node above the active region for lateral current and optical confinement. Two intermediate n-doped mirrors are inserted between the active region and the bottom mirror, forming a three-cavity cascaded structure with two passive cavities. Each intermediate mirror consists of upper and lower DBR sections separated by a 4λ-thick phase layer. The first intermediate mirror comprises 7 and 11 DBR pairs in its upper and lower sections, respectively, whereas the second comprises 9.5 and 12.5 pairs, respectively. Two approximately 2 μm-thick cavity spacers define the passive cavities, which serve as optical reservoirs for photon storage. The top mirror consists of 23 pairs of p-doped quarter-wave $Al_{0.16}Ga_{0.84}As/Al_{0.92}Ga_{0.08}As$ DBRs.

Device fabrication

The epitaxial wafer was processed using a standard top-emitting VCSEL fabrication flow. A ring-shaped Ti/Pt/Au p-type ohmic contact was first deposited on the p-contact layer surrounding the emission aperture. Mesa structures were subsequently defined by inductively coupled plasma reactive ion etching (ICP-RIE) to expose the high-Al-content oxidation layer. Lateral current confinement was realized by selective wet oxidation in an H_2O/N_2 ambient at 400 °C, producing oxide apertures with a diameter of approximately 3.5 μm. A SiO_2 passivation layer was then deposited by plasma-enhanced chemical vapor deposition (PECVD) to provide electrical isolation. After opening the contact windows, a thick Au layer was electroplated to reduce the series resistance and serve as the bonding pad. The GaAs substrate was mechanically thinned to ~200 μm, followed by deposition of a Ge/Ni/Au n-type ohmic contact on the wafer backside. Rapid thermal annealing was finally performed to improve the contact resistance. During fabrication, surface gratings were defined with a 28 nm etch depth, 880 nm period, and a 60% duty cycle.

Measurements

Cross-sectional specimens were prepared using a dual-beam focused ion beam (FIB) system (ZEISS Crossbeam 540), and the device microstructure was examined by transmission electron microscopy (FEI Talos F200X G2). The current-voltage-light output (L-I-V) characteristics,

power conversion efficiency (PCE), and far-field emission patterns were measured with a manual probe station (MPS200-UD). Polarization properties were characterized using a polarization-resolved optical measurement system, while the emission spectra were recorded with an optical spectrum analyser (Yokogawa AQ6370E). The frequency-noise power spectral density was measured using an automated cross-correlation homodyne laser noise analyser (OEwaves OE4000), while the relative intensity noise (RIN) was characterized using a laser noise analyser (OEwaves OE4001).

Optical heterodyne linewidth measurement

The laser linewidth was measured using an optical heterodyne setup. The supercavity laser was driven by a low-noise current source (LDC200CV, Thorlabs) and temperature-controlled using a thermoelectric controller (TED200C, Thorlabs). Its output was combined with that of a narrow-linewidth ECDL using a non-polarizing 50:50 beamsplitter. The combined signal was coupled into a 780HP single-mode fibre and detected by a 5-GHz InGaAs photodetector (DET08CFC/M, Thorlabs).

The resulting beat signal was recorded using a CXA signal analyser (N9000B-503, Keysight Technologies), with the beat frequency set between 100 and 300 MHz. Spectra were acquired over a 10-MHz span with a resolution bandwidth of 30 kHz, a video bandwidth of 10 kHz and five-trace averaging. The linewidth was extracted by Lorentzian fitting over a ±1.2 MHz interval centred on the beat-note frequency. Representative measurements were repeated with resolution bandwidths of 10–100 kHz to exclude analyser-limited broadening.

Optical-power and frequency-stability measurements

The supercavity laser was driven by a low-noise dc source and directly modulated at 4.6 GHz through a bias tee using an analogue signal generator (N5181B, Keysight Technologies). The microwave source was referenced to a tunable 10-MHz temperature-compensated crystal oscillator (TCXO). The modulated laser output was transmitted through a temperature-controlled Cs vapour cell and detected using a silicon photodiode (DET36A2, Thorlabs) followed by a low-noise transimpedance amplifier (DLPCA-200, FEMTO). The detected dc component was recorded using a data-acquisition unit to monitor the optical-power stability,

whereas the atomic-resonance error signal was fed back to a servo controller to stabilize the microwave frequency by tuning the TCXO. The selected signal generator and bias tee cover the required 4.6-GHz modulation frequency. The stabilized 10-MHz TCXO output was compared with a 10-MHz Cs frequency standard using a phase-noise and frequency-stability analyser. Optical power and fractional frequency were recorded simultaneously for 260,000 s using a 1-s acquisition interval. The overlapping Allan deviation was calculated from the continuously recorded fractional-frequency data using Stable32 frequency-stability analysis software, without smoothing, interpolation or linear-drift removal. The 53100A supports direct frequency-difference and Allan-deviation measurements of high-stability RF sources.

Laser linewidth analysis based on frequency-noise spectra

The laser linewidth was evaluated from the frequency-noise power spectral density (PSD), Sν(f), which characterizes the frequency fluctuations as a function of Fourier frequency. Assuming negligible amplitude noise, the optical spectrum is determined by the Fourier transform of the field autocorrelation function[26]

$$S_E(v) = E_0^2 \int_0^{\infty} cos[\,2\pi(v - v_0)\tau] \times exp[-4\int_0^{\infty} S_v(f)\frac{sin^2(\pi f\tau)}{f^2}df]d\tau \qquad (20)$$

Frequency-noise components above the β-separation line,

$$S_v(f) = \frac{8\,ln\,2}{\pi^2}f \qquad (21)$$

predominantly determine the central linewidth, whereas those below this boundary mainly contribute to the spectral wings. At sufficiently high Fourier frequencies, where the PSD reaches a white-noise floor, the laser spectrum approaches a Lorentzian profile with an intrinsic linewidth.

$$\Delta v_L = \pi S_v^{white} \qquad (22)$$

where S_v^{white} is the white-noise level in Hz^2/Hz. In this work, the intrinsic linewidth was extracted directly from the high-frequency white-noise floor of the measured frequency-noise PSD.

References

1. Pan, G., Xun, M., Zhou, X., Sun, Y. & Dong, Y. Harnessing the capabilities of VCSELs : unlocking the potential for advanced integrated photonic devices and systems. *Light Sci. Appl.* **13**, 229 (2024).
2. Liu, A., Wolf, P., Lott, J. A. & Bimberg, D. Vertical-cavity surface-emitting lasers for data communication and sensing. *Photonics Res.* **7**, 121–136 (2019).
3. Ghods, A., Dummer, M. & Johnson, K. Polarization-stable single-mode multi-junction VCSELs with integrated anti-phase mode filter. *J. Appl. Phys.* **134**, 213103 (2023).
4. Lindner, J. *et al.* 795 nm Multi-Junction Vertical-Cavity Surface-Emitting Lasers. *IEEE J. Sel. Top. Quantum Electron.* **32**, (2026).
5. Li, Y. *et al.* High-Gain InAlGaAs Quaternary Quantum Wells for High-Power 760 nm Two-Junction VCSELs. *IEEE J. Quantum Electron.* **59**, 1–8 (2023).
6. Lu, H., Alkhazragi, O. & Lin, H. Shaping the light of VCSELs through cavity geometry design. *Light Sci. Appl.* **14**, 344 (2025).
7. Zhang, C., Li, H. & Liang, D. Antireflective vertical-cavity surface-emitting laser for LiDAR. *Nat. Commun.* **15**, 1105 (2024).
8. Zhao, F., Li, Y., Tang, Z., Ren, A. & Wu, J. High-power, multi-junction, 905nm vertical-cavity surface-emitting laser with an AlGaAsSb electron-blocking layer. *Opt. Lett.* **48**, 2142–2145 (2023).
9. Pan, G. *et al.* High Slope Efficiency Bipolar Cascade 905nm Vertical Cavity Surface Emitting Laser. *IEEE Electron Device Lett.* **42**, 1342–1345 (2021).
10. Hu, S., Zhang, X., Li, C. & Yin, H. Latest advances in VCSEL technology for next-generation data center network [Invited]. **22**, 1–12 (2024).
11. Dummer, M., Johnson, K., Rothwell, S., Tatah, K. & Hibbs-Brenner, M. K. The role of VCSELs in 3D sensing and LiDAR. In *Optical Interconnects XXI* (ed. Schröder, H.) **11692**, 42–55 (SPIE, 2021).
12. Zhang, J., Zheng, W. & Liu, A. Polarized Vertical-Cavity Surface-Emitting Laser Arrays With Asymmetrical Structures for Three-Dimensional Sensing With Polarization Imaging. *IEEE J. Quantum Electron.* **59**, 1–8 (2023).
13. Huang, M., Serkland, D. K. & Camparo, J. A narrow-linewidth three-mirror VCSEL for atomic devices. *Appl. Phys. Lett.* **121**, 114002 (2022).
14. Ghods, A., Yeo, M., Gariano, J., Lawal, W. & Agrawal, S. Advanced Characterization of 795nm VCSELs for Atomic Clock Applications. vol, 13451 1–5 (SPIE, 2025).
15. Zhou, P. *et al.* Application of VCSEL in Bio-Sensing Atomic Magnetometers. *Biosens. Rev.* **12**, 1098 (2022).
16. Kitching, J. Chip-scale atomic devices. *Appl. Phys. Rev.* **5**, 031302 (2018).
17. Cui, N. *et al.* 2.46 MHz Ultranarrow Line Width Vertical-Cavity Surface-Emitting Lasers with

Cholesteric Liquid Crystals Coupled Cavity. *ACS Photonics* **12**, 737–746 (2025).

18. Xun, M. *et al.* Longitudinal Multi-Cavity Coupled VCSELs With Narrow Linewidth and High Single Mode Power for Quantum Sensing. *J. Light. Technol.* **42**, 5949–5955 (2024).

19. Tang, Z. *et al.* Vertical-Cavity Surface-Emitting Laser Linewidth Narrowing Enabled by Internal-Cavity Engineering. *IEEE J. Quantum Electron.* **60**, 1–8 (2024).

20. Serkland, D. K., Chow, W. W., Geib, K. M. & Peake, G. M. Final Report on LDRD Project: Narrow-Linewidth VCSELs for Atomic Microsystems, Report No. SAND2011-7089 (Sandia National Laboratories, 2011)

21. Serkland, D. K., Keeler, G. A., Geib, K. M. & Peake, G. M. Narrow linewidth VCSELs for high-resolution spectroscopy. In *Vertical-Cavity Surface-Emitting Lasers XIII* (eds Choquette, K. D. & Lei, C.) **7229**, 72290A (SPIE, 2009).

22. Tang, Z. *et al.* 1-MHz linewidth VCSEL enabled by monolithically integrated passive cavity for high-stability chip- scale atomic clocks. *Light Sci. Appl.* **15**, 94 (2026).

23. Ingfei, J. M. U. *et al.* 5.3 mW at 80°C, single-mode high-power 795 nm VCSEL achieved solely through intracavity design. *Opt. Express* **33**, 23865–23872 (2025).

24. Zhou, X. *et al.* High-Power Low-Divergence Single-Mode Multi-Junction Cascade VCSELs. *IEEE Trans. Electron Devices* **71**, 5472–5476 (2024).

25. Xiao, Y. *et al.* Twenty-milliwatt, high-power, high-efficiency, single-mode, multi-junction vertical-cavity surface-emitting lasers using surface microstructures. *Photonics Res.* **12**, 1899 (2024).

26. Tran, M. A., Huang, D. & Bowers, J. E. Tutorial on narrow linewidth tunable semiconductor lasers using Si/III-V heterogeneous integration. *APL Photonics* **4**, 111101 (2019).

27. Zhang, J. *et al.* High-power vertical external-cavity surface-emitting laser emitting switchable wavelengths. *Opt. Express* **28**, 32612 (2020).

28. Jiang, L. *et al.* Ultra-narrow linewidth vertical-cavity surface-emitting laser based on external-cavity weak distributed feedback. *Opt. Express* **30**, 37519 (2022).

29. Huang, W. *et al.* Kilohertz linewidth VCSEL with an external high Q-factor intrinsic optical fiber Fabry-Pérot cavity. *Opt. Express* **34**, 20611–20620 (2026).

30. Jin, L. *et al.* Narrow linewidth VCSEL self-injection-locked to a microresonator with a two-fiber coupler. *Opt. Lett.* **50**, 6461–6464 (2025).

31. Serkland, D. K. *et al.* Mode selection and tuning of single-frequency short-cavity VECSELs. in *Vertical-Cavity Surface-Emitting Lasers XXII, 1055206* vol. 10552 5 (2018).

32. Henry, C. H. Theory of the Linewidth of Semiconductor Lasers. *IEEE J. Quantum Electron.* **18**, 259–264 (1982).

33. Kippenberg, T. J. A. Nonlinear Optics in Ultra-high-Q Whispering-Gallery Optical Microcavities. PhD thesis, California Institute of Technology (2004), p. 24.

34. M. A. Tran. *et al.* Ring-Resonator Based Widely-Tunable Narrow-Linewidth Si/InP Integrated Lasers. *IEEE J. Sel. Top. Quantum Electron.* **26**, 1–14 (2020).

35. Coldren, L. A., Corzine, S. W. & Mašanović, M. L. *Diode Lasers and Photonic Integrated Circuits* 2nd edn (Wiley, 2012).

36. Xiang, L. *et al.* Stable single-mode operation of 894.6 nm VCSEL at high temperatures for Cs atomic sensing. *Chinese Phys. B* **26**, 3–7 (2017).

37. Uehui, Y. X. U. *et al.* Single-mode VCSELs utilizing annular metal apertures for lateral confinement and on-chip beam shaping techniques. *Opt. Express* **33**, 46494–46506 (2025).

38. Cui, Y. *et al.* Single-mode chirped high-contrast metastructure VCSEL for 106 Gbps PAM4 transmission. *Optica* **11**, 1567 (2024).

39. Hou, Y. I. Z. *et al.* Large-aperture single-mode 795 nm VCSEL for chip-scale nuclear magnetic resonance gyroscope with an output power of 4 . 1 mW at 80 ° C. **30**, 8991–8999 (2022).

40. An, G. U. P. *et al.* Design , fabrication , and nanosecond-pulse characterization of high-power-density multi-junction VCSEL arrays. *Opt. Express* **33**, 44811–44820 (2025).

41. Zhang, X. *et al.* High-fundamental-mode output of 1064 nm vertical-cavity surface-emitting laser using double embedded antiresonant oxide islands. *Inf. Funct. Mater.* **2**, 118–129 (2025).

42. Di Domenico, G., Schilt, S. & Thomann, P. Simple approach to the relation between laser frequency noise and laser line shape. *Appl. Opt.* **49**, 4801–4807 (2010).

43. Gruet, F. *et al.* Metrological characterization of custom-designed 894.6 nm VCSELs for miniature atomic clocks. *Opt. Express* **21**, 467–478 (2013).

44. Lian, J. *et al.* CPT chip-scale atomic clock with direct-modulation chip- external cavity diode laser. *Appl. Phys. Lett.* **126**, 224002 (2025).

45. Larsson, A. Advances in VCSELs for communication and sensing. *IEEE J. Sel. Top. Quantum Electron.* **17**, 1552–1567 (2011).

Supplementary Files

This is a list of supplementary files associated with this preprint. Click to download.

- SupplemenraryInformation.docx